Monthly Notices of the ROYAL ASTRONOMICAL SOCIETY
MNRAS **511,** 3113–3124 (2022) https://doi.org/10.1093/mnras/stab3660

The nature of the Cygnus extreme B supergiant 2MASS J20395358+4222505

A. Herrero [1,2★] S. R. Berlanas [3★] A. Gil de Paz [4,5] F. Comerón,[6] J. Puls,[7] S. Ramírez Alegría [8] M. Garcia [9] D. J. Lennon,[1,2] F. Najarro,[9] S. Simón-Díaz,[1,2] M. A. Urbaneja,[10] J. Gallego,[4,5] E. Carrasco [11] J. Iglesias,[12] R. Cedazo,[13] M. L. García Vargas [14] Á. Castillo-Morales,[4,5] S. Pascual,[4,5] N. Cardiel [4,5] A. Pérez-Calpena,[14] P. Gómez-Alvarez[14] and I. Martínez-Delgado[14]

[1]*Instituto de Astrofísica de Canarias, 38200, La Laguna, Tenerife, Spain*
[2]*Departamento de Astrofísica, Universidad de La Laguna, 38205, La Laguna, Tenerife, Spain*
[3]*Departamento de Física Aplicada, Facultad de Ciencias II, Universidad de Alicante, Spain*
[4]*Departamento de Física de la Tierra y Astrofísica, Universidad Complutense de Madrid, E-28040, Madrid, Spain*
[5]*Instituto de Física de Partículas y del Cosmos IPARCOS, Fac. de Ciencias Físicas, Univ. Complutense de Madrid, E-28040, Madrid, Spain*
[6]*European Southern Observatory, Karl Schwarzschild Str. 2, 85748, Garching, Germany*
[7]*LMU München, Universitätssternwarte, Scheinerstr. 1, 81679 München, Germany*
[8]*Centro de Astronomía (CITEVA), Universidad de Antofagasta, Av. Angamos 601, Antofagasta, Chile*
[9]*Centro de Astrobiología, CSIC-INTA, Ctra de Torrejón a Ajalvir km 4, E-28850 Torrejón de Ardoz, Madrid, Spain*
[10]*Institut für Astro- und Teilchenphysik, Universität Innsbruck, Technikerstr. 25/8, 6020 Innsbruck, Austria*
[11]*Instituto Nacional de Astrofísica, Óptica y Electrónica, Luis Enrique Erro No. 1, C.P. 72840, Tonantzintla, Puebla, México*
[12]*Instituto de Astrofísica de Andalucía (CSIC), Apdo. 3004, E-18008, Granada, Spain*
[13]*Departamento de Ingeniería Eléctrica, Electrónica Automática y Física Aplicada, E.T.S. de Ingeniería y Diseño Industrial, Rda. de Valencia, 3, E-28012, Madrid, Spain*
[14]*Fractal, S.L..N.E., Calle Tulipán 2, portal 13, 1A, E-28231 Las Rozas de Madrid, Spain*

Accepted 2021 December 9. Received 2021 November 30; in original form 2021 September 29

ABSTRACT

2MASS J20395358+4222505 is an obscured early B supergiant near the massive OB star association Cygnus OB2. Despite its bright infrared magnitude ($K_s = 5.82$) it has remained largely ignored because of its dim optical magnitude ($B = 16.63$, $V = 13.68$). In a previous paper, we classified it as a highly reddened, potentially extremely luminous, early B-type supergiant. We obtained its spectrum in the *U*, *B* and *R* spectral bands during commissioning observations with the instrument MEGARA at the Gran Telescopio CANARIAS. It displays a particularly strong H_α emission for its spectral type, B1 Ia. The star seems to be in an intermediate phase between supergiant and hypergiant, a group that it will probably join in the near (astronomical) future. We observe a radial velocity difference between individual observations and determine the stellar parameters, obtaining $T_{\rm eff} = 24\,000$ K and $\log g_c = 2.88 \pm 0.15$. The rotational velocity found is large for a B supergiant, $v \sin i = 110 \pm 25$ km s^{-1}. The abundance pattern is consistent with solar, with a mild C underabundance (based on a single line). Assuming that J20395358+4222505 is at the distance of Cyg OB2, we derive the radius from infrared photometry, finding $R = 41.2 \pm 4.0$ $R_\odot$, $\log(L/L_\odot) = 5.71 \pm 0.04$ and a spectroscopic mass of 46.5 ± 15.0 $M_\odot$. The clumped mass-loss rate (clumping factor 10) is very high for the spectral type, $\dot{M} = 2.4 \times 10^{-6}$ $M_\odot$ a^{-1}. The high rotational velocity and mass-loss rate place the star at the hot side of the bi-stability jump. Together with the nearly solar CNO abundance pattern, they may also point to evolution in a binary system, J20395358+4222505 being the initial secondary.

Key words: stars: evolution – stars: individual: 2MASS J20395358+4222505 – stars: massive – supergiants – stars: winds, outflows.

1 INTRODUCTION

Massive stars are a tiny fraction of a given stellar generation. For a Salpeter initial mass function (IMF) we expect only one star with more than eight solar masses for every 500 stars of smaller mass. Moreover, they are the first members of that generation to evolve and disappear in only a few tens of millions of years, when solar-type stars barely begin their life in the main sequence. As a consequence, massive stars are scarce objects in the Universe. Their study is additionally complicated by the fact that they are relatively far away (compared with stars of lower mass), tend to be born in binary or multiple systems (Sana et al. 2012; de Mink et al. 2013), are associated with dense clouds of interstellar material from which they were born, or are new stars in the process of formation (Motte, Bontemps & Louvet 2018). Thus, the number of objects available for detailed observation and analysis is comparatively scant.

★ E-mail: ahd@iac.es (AH); sara.rb@ua.es (SB)

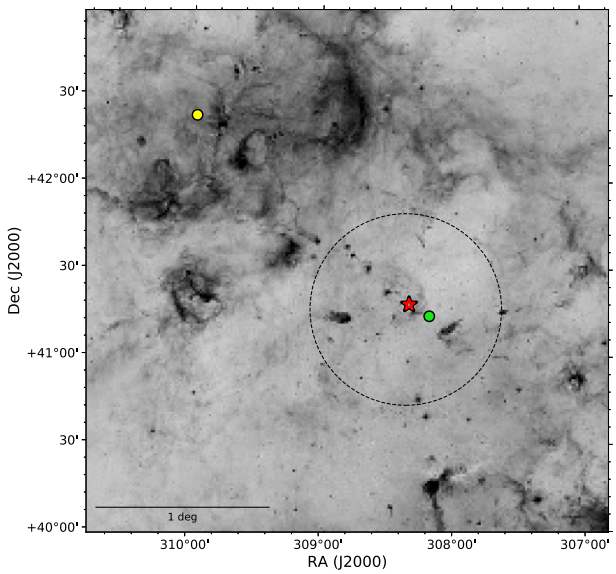

Figure 1. The region of the Cyg OB2 association showing the location of J20395358+4222505 (yellow dot). The red star marks the position of the Cyg OB2 #8 multiple stellar system, which may be considered the centre of the association, and the green circle represents Cyg OB2 #12. The dashed circle indicates the core of the association as defined by Wright et al. (2015).

Among massive stars, blue hypergiants and extreme supergiants are a rare stage because they have high luminosities and are of very short duration (see, e.g. Clark et al. 2012). Also, they are crucial to understand the evolutionary channels followed by single and multiple massive stars, from O and B stages to luminous blue variables (LBVs), red supergiants (RSGs) and Wolf–Rayets (WRs), and ultimately to the end products of massive star evolution: supernovae (SNe), neutron stars (NSs), black holes (BHs), high-mass X-ray binaries, long-duration gamma ray bursts (GRBs) and gravitational wave progenitors (e.g. Langer 2012; Abbott et al. 2016).

Here we report on 2MASS J20395358+4222505 (Skrutskie et al. 2006),[1] a highly reddened object in the vicinity of the Cygnus OB2 association (see Fig. 1). It was spectroscopically observed by Berlanas et al. (2018) and classified as B0 I. These authors quote an apparent magnitude in the B band of $m_B = 15.89$ (Comerón & Pasquali 2012) and estimate an extinction of $A_v = 11$ for this star or $A_B \approx 14.6$. Adopting a distance of 1.76 kpc to Cyg OB2 (Berlanas et al. 2018), this implies an absolute magnitude $M_V \approx -9.8$, or, adopting a Bolometric Correction (B.C.) $= -2.0$, $M_{\rm bol} \approx -11.8$ and $\log L/L_\odot \approx 6.6$.[2] This would place the star as one of the most luminous objects among the B supergiants, comparable to the B hypergiants listed by Clark et al. (2012). In this paper, we present new observations of J20395358+4222505 obtained with MEGARA at the 10.4-m Gran Telescopio CANARIAS (GTC) and a first analysis to obtain its stellar parameters.

[1]Comerón & Pasquali (2012) identify it as J20395358+4222506. Both entries return the same data in the 2MASS catalogue, and it is the only source within 5 arcsec

[2]This value is different from the one obtained in this work because we have used infrared photometry to determine the radius instead of the B magnitude. Note also that the B magnitude quoted by Comerón & Pasquali (2012) from NOMAD is different from the one adopted here from UCAC4. See Section 4.2.

2 OBSERVATIONS

The observations were carried out with the MEGARA integral-field and multi-object fibre spectrograph (Gil de Paz et al. 2018) during its commissioning phase at the GTC on the nights of 2017 August 29 and 30. The integral-field unit called the large compact bundle (LCB hereafter) was used for these observations. The LCB fully covers a field of view of 12.5 × 11.3 arcsec^2 with a total of 567 hexagonal spaxels of 0.62 arcsec (diameter of the circle on which the spaxel is inscribed) plus 56 spaxels split in the eight seven-fibre minibundles located at ∼2 arcmin from the LCB centre, which are used for accurate simultaneous sky subtraction. J20395358+4222505 was observed with three different volume phase holographic gratings, namely LR-U, LR-B and HR-R. These set-ups yielded the wavelength coverage specified in Table 1. The LR-B set-up was observed on 2017 August 29, while the other two set-ups were observed on 2017 August 30. The on-target exposure times and resolving powers achieved are also listed in Table 1, together with the signal-to-noise ratio (S/N). The use of the LCB IFU avoided losing any flux from the star due to small pointing errors (3.5 arcsec in the case of the LR-B observations on 2017 August 29) or bad seeing (1 arcsec on 2017 August 29 but between 1.5 and 2 arcsec on 2017 August 30).

The data reduction was done using the Python-based MEGARA Data Reduction Pipeline (Cardiel & Pascual 2018; Pascual et al. 2019). The data processing included the bias subtraction for each of the two amplifiers used for reading out the MEGARA E2V 231-84 CCD, the trimming of the image section of the CCD, tracing the fibres, wavelength calibration, fibre-flat fielding, and flux calibration. The wavelength calibration was performed using ThAr lamps for the LR-U and LR-B set-ups and ThNe lamps for HR-R. The flux calibration was obtained by observing the spectro-photometric standard stars Feige 15 and BD+40 4032. The processing of the images in each spectral set-up was done separately and yielded three different flux-calibrated multi-extension row-stacked-spectra (RSS hereafter) FITS frames that include 623 4300-element flux vectors and positions on the sky of every single fibre. A faint extended nebulosity is seen in some fibres away from the star, producing faint nebular lines, such as O III, S II, N II or H_α. However, the reduced stellar spectra do not show indications of their presence, or over/undersubtraction.

After data reduction, the LR-U and LR-B spectra were degraded to $R = 3000$ to improve the S/N and all spectra were shifted to the rest frame by correcting for individual radial velocity offsets. The LR-B spectrum, taken on 2017 August 29, required a larger correction than the LR-U and HR-R spectra taken the day after (with a difference in radial velocity of about 60 km s^{-1} between the first spectrum and the other two when correcting them to the rest frame). We tried to confirm the variation by looking at the interstellar medium (ISM) features. The HR-R spectrum, of better quality, shows ISM lines consistent with the velocity of stellar lines and with their rest frame, as listed by Herbig (1995). The interstellar Ca II lines can be identified in the LR-U spectrum with a velocity that is also consistent with their laboratory wavelength and a small shift of 20 ± 14 km s^{-1} with respect to the stellar lines. The situation is more difficult in the LR-B spectrum, which shows a number of strong interstellar features that are however relatively broad. They are again consistent with their rest frame, although with a larger error bar (10 ± 17 km s^{-1}) but show a large shift (68 ± 23 km s^{-1}) with respect to the stellar lines, as we would expect if the star is moving with respect to the ISM; however, the ISM radial velocities in LR-B are not fully consistent with those of the HR-R and LR-U spectra after barycentric correction, with a

Table 1. Details of the observations with the different gratings. Wavelengths are in Angstroms and exposure times in seconds. The S/N in the LR-U grating does not include the bluemost wavelengths, which have a poorer signal.

Grating	Central wavelength	Spectral range	Resolving power	Exposure time	S/N
LR-U	4025.90	3654.32–4391.88	5750	2700	40–55
LR-B	4785.32	4332.05–5199.96	5000	1800	40–75
HR-R	6602.59	6405.61–6797.14	20 050	900	110

difference of 22 ± 19 km s^{-1}. For this reason, with only one set of spectra for each wavelength range, we refrain from speculating about the properties of the putative binary and will only consider its possible presence when discussing some points in Sections 4.2, 4.3 and 4.5.

3 SPECTROSCOPIC ANALYSIS

3.1 General description

Fig. 2 shows the observed spectrum, together with the final fit described in the next section, and the main spectroscopic features marked. We identify clearly the Balmer series with the strong emission in H_α and also a very weak red emission peak in H_β.[3] The He I lines are strong and He II λ4686 is weak but marginally present, and probably blended with a weak Si III 4683 line. A weak Mg II λ4481 line is also seen. The Si spectrum is clear with a strong Si III triplet at λλ4552-67-75 and weak Si IV lines at λ4089 and λ4116, the former being blended with an O II line. No Si II lines could be identified. The N spectrum displays the N III lines around λ4640 and for N II only the very faint lines at λλ 5005–5007 Å could be identified. The C spectrum is also not very remarkable, although the C II lines at λ6578-83 Å are clearly present. The region around λ4650 is dominated by the O II lines, and shows a rich spectrum.

We classify the star using the silicon reference frame for the classification of B-type supergiants described by Walborn & Fitzpatrick (1990). Specifically, the spectral type is defined by the ratio of Si IV 4089 to Si III 4552 that indicates a spectral type of B1. A luminosity class of Ia is indicated by the weakness of the H_γ and H_β beta lines, so the star is classified as B1 Ia. In spite of the strong H_α emission, it does not show a clear P-Cygni profile in H_β, as do all early-B Ia$^+$ stars in Clark et al. (2012). Therefore, we do not classify it as Ia$^+$, but the star is clearly close to that regime. We suggest that the presence of a P-Cygni profile in H_β could be used to distinguish classes Ia and Ia$^+$, presently not clearly separated. This way, a purely spectroscopic criterion would be used, which will strengthen the objectivity in the classification. The presence of He II 4686 in the spectrum, while it is very weak, is slightly peculiar, although it is well fitted by the synthetic spectrum (see Fig. 2). Either it may indicate helium enrichment or it might be a result of the high stellar luminosity, as discussed below.

In Fig. 3, we compare selected regions of the spectrum of J20395358+4222505 with those of the BC0.7 Ia supergiant HD 2905 (κ Cas)[4] from the IACOB data base (Simón-Díaz et al. 2011, 2020), degraded to the same resolving power as J20395358+4222505. HD 2905 has been recently analysed by Simón-Díaz et al. (2018). The comparison of the He I 4471Å and Mg II 4481Å lines indicates a similar temperature for both stars.[5] This is confirmed by the behaviour of the Si III lines at 4552-72Å. The Si IV lines around H_δ are slightly weaker in the case of J20395358+4222505, whereas He II 4686Å, weak in HD 2905, is marginally present in J20395358+4222505. These differences can be partly explained considering the different H_α emission of both stars, pointing to a stronger or denser stellar wind or to a slightly enriched He spectrum in J20395358+4222505, or both. The N II spectrum (particularly the line at λ4630) is similar in both stars, indicating that J20395358+4222505 could also be of BC type, but we will wait for a better spectrum to confirm this nuance. The behaviours of H_δ and H_γ are not completely consistent, perhaps affected by the strong wind producing the H_α emission or by the noise in the region of H_δ, but they point to a similar gravity. We also show in the figure the H_α emission of the hypergiant CygOB2 #12 (B3-4 Ia$^+$) obtained by A. Pellerin with the High Resolution Spectrograph at the Hobby-Eberly Telescope (again degraded to compare with J20395358+4222505; an analysis of Cyg OB2 #12 and other blue hypergiants can be found in Clark et al. 2012). This illustrates that the H_α emission in J20395358+4222505 is indeed very strong and broad. From this comparison, we expect the stellar parameters of J20395358+4222505 to be similar to those of HD 2905, but with a stronger stellar wind.

3.2 Stellar parameters

We have determined the projected rotational velocity and the extra broadening (so-called macroturbulence, Θ) from Si III λ4552 Å (at $R = 3000$ and in the original $R = 6000$ spectrum), He I 4713 Å (at $R = 3000$) and He I 6678 Å (at $R = 20\,050$) [6] using the IACOBBROAD package (see Simón-Díaz & Herrero 2014), which uses both a Fourier transform and a goodness-of-fit technique to determine these values, assuming a classical rotational and a radial-tangential profile (see Gray 2008).

All lines gave consistent results, and we obtained $v \sin i = 110 \pm 25$ km s^{-1} and $\Theta_{RT} = 86 \pm 30$ km s^{-1}.

This is a large rotational velocity for a B supergiant, doubling that of HD 2905 (Simón-Díaz et al. 2018) or the highest one in the sample of Clark et al. (2012) (BP Cru, 55 km s^{-1}). We can speculate that the high mass-loss rate found in Section 4.4 is a recent phenomenon, otherwise the star should have slowed down. Alternatively, it may indicate an efficient transport of angular momentum from the interior to the surface.

We have used the atmosphere code FASTWIND (Santolaya-Rey, Puls & Herrero 1997; Puls et al. 2005; Rivero-González,

[3]The strong diffuse interstellar band redwards of H_β could however mask a faint red emission in this case. Note the weak emission in the synthetic spectrum at this point

[4]κ Cas appears to be classified as B1 Ia in Simbad (Lesh 1968). Walborn (1972) classified it as BC0.7Ia. Because of its Si IV to Si III ratio and lack of P-Cygni profile in H_β, we agree with the classification by Walborn

[5]Clark et al. (2012) indicate that this ratio may depend on the location of the transition region between photosphere and wind. We run some models to test the effect, concluding that this line ratio is not affected in the case of J20395358+4222505.

[6]In spite of the Stark broadening, the low gravity combined with the high v sin *i* render He I lines useful for this purpose

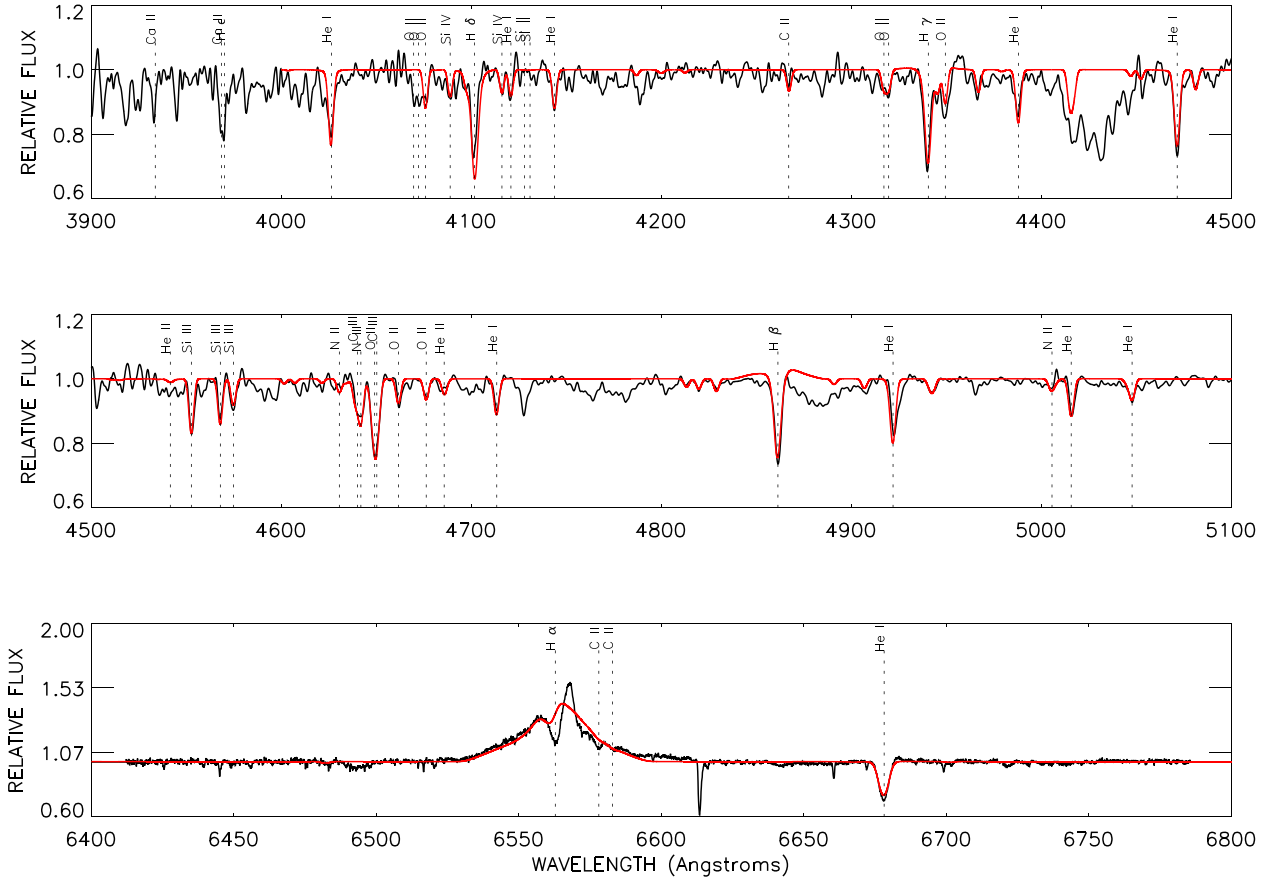

Figure 2. The spectrum of the B hypergiant J20395358+4222505 observed with MEGARA at the GTC together with our final fit (see Section 3.2). The violet and blue wavelength ranges have been degraded to $R = 3000$, whereas the original $R = 20\,050$ has been kept for the H_α region. The main lines used in the analysis have been identified for reference.

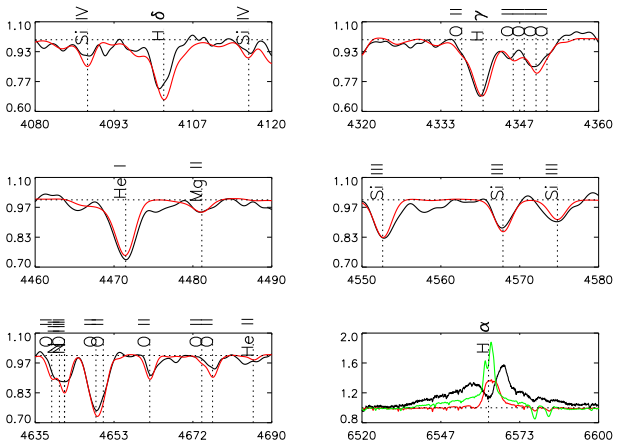

Figure 3. Comparison of the spectrum of J20395358+4222505 (B1 Ia, black) with that of HD 2905 (BC0.7 Ia, red) and Cyg OB2 #12 (B3-4 Ia^+, green, only in the H_α range) in selected spectral regions. See text for a discussion. The abcissa is the wavelength in Angstroms and the ordinate is the relative flux.

Puls & Najarro 2011) to estimate the stellar parameters of J20395358+4222505. FASTWIND calculates the emergent stellar spectrum in spherical geometry with mass loss and non-local thermodynamic equilibrium conditions. Because of the relatively low S/N of our spectrum in the blue–violet region and the large parameter space, we carry out an estimation of the stellar parameters looking by eye for the model that best fits all diagnostics simultaneously, rather than using our semi-automatic tools. Uncertainties are estimated by varying the stellar parameters until we find that the fit is not acceptable. A more accurate determination of stellar parameters and errors will be carried out in the future when higher S/N spectra are available.

The effective temperature is mainly constrained by the Si III–IV and He I–II balances and the He I 4471 to Mg II 4481 ratio. The gravity is mainly derived from the fit to the wings of the higher Balmer lines (H_γ and H_δ; H_ϵ is not used because of the low S/N in the region). After the comparison with HD 2905, we give slightly more weight to H_γ. The mass-loss rate is obtained from H_α and H_β. The strong emission in H_α allows us to exceptionally constrain the terminal wind velocity and the exponent of the wind velocity law β from the optical spectrum, and thus we obtain $v_\infty = 1500 \pm 200$ km s^{-1} and $\beta = 1.2 \pm 0.1$. The microturbulence has been set to 20 km s^{-1} under the initial assumption that the silicon abundance is solar. This value is close to the one obtained by Simón-Díaz et al. (2018) of 19 km s^{-1} for HD 2905. These authors do not consider clumping, and thus we have used the analysis of blue hypergiants made by Clark et al. (2012) as a reference. We have adopted a clumping parameter[7] $f_{\rm cl} = 10$, intermediate between the values given by Clark et al. (2012) for Cyg

[7]Note that FASTWIND and CMFGEN, the code used by Clark et al. (2012), characterize clumping in different ways: either in the form of a clumping factor (FASTWIND; $f_{\rm cl} = \langle\rho^2\rangle/(\langle\rho\rangle^2)$) or a volume filling factor (CMFGEN), which under typical assumptions are inverse to each other, $f_{\rm cl} = f_v^{-1}$ as it has been assumed above when giving the numbers of Clark et al.

Table 2. Stellar parameters for J20395358+4222505. The stellar mass has been calculated with the gravity corrected for centrifugal acceleration (note that the radius enters in this correction). The whole set of values is given for the adopted distance, together with the statistical errors of the analysis. For parameters depending on the distance, we give the values corresponding to the extreme lower and upper distances. Similar statistical errors would apply to them. No error is given for the adopted value of microturbulence. The wind parameter $Q = \dot{M}/[(v_\infty R)^{3/2}]$ and the modified wind momentum, $D_{\rm mom} = \dot{M}\ v_\infty (R_*/R_\odot)^{0.5}$, are given in cgs. units. The latter is discussed in Section 4.4. See text for other details.

Parameter	Adopted distance (1.76 kpc)	Range of distances (1.5–2.3 kpc)
$v \sin i$ (km s^{-1})	110 ± 25	
$\Theta_{\rm RT}$ (km s^{-1})	86 ± 30	
$T_{\rm eff}$ (K)	$24\,000 \pm 500$	
log g (dex cgs)	2.85 ± 0.15	
log $g_{\rm c}$ (dex cgs)	2.88 ± 0.15	2.88–2.87
logQ (dex cgs)	-12.81 ± 0.10	
ξ (km s^{-1})	20.	
$\epsilon =$ N(He)/[N(H) + N(He)]	0.12 ± 0.04	
β	1.2 ± 0.1	
v_∞ (km s^{-1})	1500 ± 200	
$R/{\rm R}_\odot$	41.2 ± 4.0	34.6–53.5
log($L/{\rm L}_\odot$)	5.71 ± 0.04	5.55–5.93
$M_{\rm bol}$ (mag)	-9.52 ± 0.10	-9.14 to -10.09
$M/{\rm M}_\odot$	46.5 ± 15.0	32.9–77.4
$\dot{M} \times 10^6$ (M$_\odot$ a^{-1})	$2.40^{+0.20}_{-0.30}$	1.8–3.6
$f_{\rm cl}$	10.	
v_1/v_∞	0.2	
v_2/v_∞	0.5	
log ($D_{\rm mom}$) (cgs)	29.16 ± 0.11	29.01–29.39

OB2#12 ($f_{\rm cl} = 25$) and HD 190603 ($f_{\rm cl} = 4$). Thus, our mass-loss rate will be equivalent to an unclumped mass-loss rate that is higher by about a factor of $\sqrt{10}$. We have adopted a linear clumping law, increasing from $f_{\rm cl} = 1$ (unclumped) at $v_1 = 0.2 v_\infty$ to $f_{\rm cl} = 10$ at $v_2 = 0.5 v_\infty$, and keeping it constant at this value until v_∞. This choice has been driven by the need to get a high emission in H$_\alpha$ while not getting too much in H$_\beta$ and H$_\gamma$. Varying these parameters modifies the quality of the fit, but does not change the other stellar parameters beyond the adopted errors.

Final stellar parameters resulting from the spectral fit are given in Table 2. Stellar radius, luminosity, mass and mass-loss rate require the distance and extinction determination, which are described in Sections 4.1 and 4.2. The final adopted fit is shown in Fig. 2 (calculated with the abundances given in Section 3.3). Spectral features are well reproduced, except H$_\alpha$ in the core and, to a lesser extent, H$_\beta$ in the wings, both very sensitive to the details of the adopted clumping law. In particular, we carried out model calculations that indicate that the central absorption in the core of H$_\alpha$ varies as a consequence of the clumping depth dependence. The core of H$_\delta$ is also not well reproduced, but H$_\gamma$, with better S/N, shows a very good fit.

3.3 Abundances

Abundances are estimated by fitting the different ions in the observed spectrum. Microturbulence is again fixed at 20 km s^{-1} for all elements, the same value adopted for the Si ionization balance. All abundances are given by number and were initially adopted to be solar and then modified to reach a better fit to the observed spectrum.

Table 3. Abundance numbers for J20395358+4222505. For reference, we also give the solar values by Asplund et al. (2009).

	log(X/H) + 12	Solar
He	11.08 ± 0.14	10.92 ± 0.01
C	$8.13^{+0.20}_{-0.25}$	8.43 ± 0.05
N	7.83 ± 0.15	7.83 ± 0.05
O	8.69 ± 0.15	8.69 ± 0.05
Mg	7.53 ± 0.15	7.60 ± 0.04
Si	7.51 ± 0.10	7.51 ± 0.03

Most He lines are well fitted with a solar abundance, but the strong He I 4471 Å line points to a slightly enriched He abundance, which is consistent with the detection of He II 4686. Thus, we adopt $\epsilon = N({\rm He})/[N({\rm H}) + N({\rm He})] = 0.12 \pm 0.04$, a mildly enriched He abundance, but still consistent with the solar one. The N abundance is poorly constrained, as the N III lines around 4630–4640 are blended with O and C and are highly sensitive to wind details (see Rivero-González et al. 2011), whereas the N II lines from 5666 to 5710, clear in this spectral type, are outside the spectral range of our observations. Thus, we have to rely on the very weak N II 5005.15 and 5007.33 Å lines (a blend in our spectrum). These lines are consistent with a solar N abundance. The absence of N II 4630.54 and N III 4634.13 (which should be present if the N abundance is higher than solar) is also consistent with a solar N abundance. Taking into account the uncertainties in stellar parameters, we determine a value of log(N/H) + 12 = 7.83 ± 0.15 (with 7.83 ± 0.05 being the solar value from Asplund et al. 2009). The abundance of C relies on the C II λ4267 line, which is weak. Unfortunately, the C II 6578-83 lines are not well reproduced by our model. We estimate a C abundance of log(C/H) + 12 = $8.13^{+0.20}_{-0.25}$, a factor of 2 below solar, where errors have again been obtained by fitting the line with varying stellar parameters. However, given the uncertainties, the line weakness and the moderate S/N in the region, we cannot completely rule out a solar abundance. For Mg we have only the doublet line at λ4481, which fits at a slightly lower than solar abundance, but fully compatible with solar – we obtain log(Mg/H) + 12 = 7.53 ± 0.15 – where the relatively low uncertainty is probably an underestimate as we have only one line available. On the contrary, for O and Si we have several lines and thus the same uncertainty of 0.15 dex is more representative. We obtain in both cases solar abundances, with uncertainties determined by varying the stellar parameters (except the microturbulence, which we kept fixed through the whole analysis). Abundances are given in Table 3.

4 DISCUSSION

4.1 Distance

The distance to J20395358+4222505 is not well determined. Based on *Gaia* Data Release 2 (DR2, Gaia Collaboration et al., 2018; Gaia Collaboration et al., 2016) measurements, Bailer-Jones et al. (2018) obtain a distance of 650 pc from its parallax of 1.54 ± 0.25 mas, whereas eDR3 (Gaia Collaboration et al., 2021) gives a parallax of 0.439 ± 0.09 mas after correcting from the zero-point (Lindegren et al. 2021), which would correspond to a plain distance of 2.28 kpc. However, both these measurements have a large renormalized unit weight error (RUWE; see Lindegren et al. 2018) that amounts to 2.88 in the first case and to 2.95 in the second. This is more than twice the maximum recommended value of 1.4. The short distance is difficult to reconcile with the high

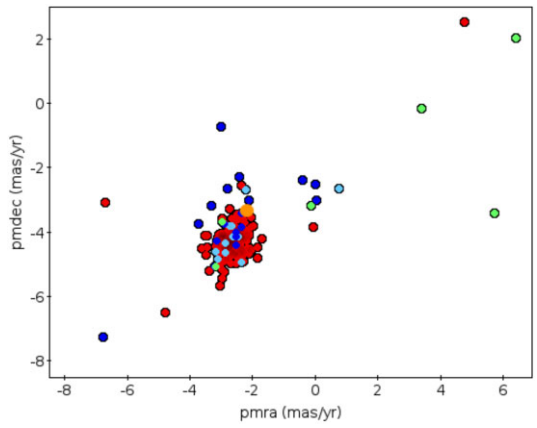

Figure 4. *Gaia* eDR3 proper motions of J20395358+4222505 (orange circle) and OB-type Cyg OB2 stars. The different colours identify the groups found by Berlanas et al. (2019): group 1 (at 1.35 kpc, blue circles); group 2 (at 1.76 kpc, red circles), group 0 (between group 1 and 2, cyan circles) and group 3 (foreground or background stars, green circles).

extinction towards this object,[8] its stellar parameters and its strong H_α emission (implying a high luminosity) and we discard it. The position of J20395358+4222505 in the sky coincides with the star-forming region DR21, located at 1.5 kpc (Rygl et al. 2012). Given the strong extinction towards J20395358+4222505, we adopt this as a lower limit for its distance. To adopt an upper limit, we rely on the recent work by Pantaleoni González et al. (2021). These authors have presented a spatial distribution of the massive stars in the solar neighbourhood. In their fig. 5, we clearly identify the stellar clustering that corresponds to the Cygnus X region and extends from 1.5 to 2.0 kpc. Beyond that distance, the stellar density decreases significantly (the Cygnus arm ends). Therefore, we adopt the distance of 2.3 kpc given by eDR3 as an upper limit, but note that there is a small probability that the star is at an even greater distance.

The Cyg OB2 association lies very close in the sky (slightly more than 1°; see Fig. 1) and a simple hypothesis would be to assume that the star belongs to the surroundings of this association and is at the same distance. This assumption is supported by the peculiar spectral type, B1 Ia, that we would expect to be associated with a massive star-forming region. However, the star is isolated, and its proper motion, ($\mu_\alpha = -2.139 \pm 0.101$ mas a^{-1}, $\mu_\delta = -3.351 \pm 0.116$ mas a^{-1}, eDR3 data) is similar to that of the main stellar group in Cyg OB2[9] and other stars in the region (see Fig. 4). This suggests that it is not a runaway, which makes its connection to Cyg OB2 less plausible. There is a possibility that the star is at a larger distance than Cyg OB2.

The distance to Cyg OB2 has been determined by different authors. Massey & Thomson (1991) and Torres-Dodgen, Tapia & Carroll (1991) place the association at 1.8 kpc based on stellar photometry and spectroscopy. Later, Hanson (2003) places it at a shorter distance of 1.5 kpc, that Negueruela et al. (2008) find consistent with their data.[10] More recently, Rygl et al. (2012) find a similar distance of 1.4 kpc on the basis of the radio parallaxes to four masers in star-forming regions close to Cyg OB2, thus indicating that this may be the distance to the whole Cygnus X region. More recently, again based on *Gaia* DR2 data, Berlanas et al. (2019) have found the existence of two groups of OB stars in Cyg OB2, a nearby one at 1.35 kpc formed by a small number of relatively dispersed objects and a second one at 1.76 kpc that includes most of the stars and can be identified with the OB association. This is consistent with the larger distance modulus found by Massey & Thomson (1991) and Torres-Dodgen et al. (1991). This value is also consistent with that found by Maíz Apellániz et al. (2020) for the two main clusters that form the main group of Cyg OB2: the Villafranca O-007 and O-008 – also identified by Bica, Bonatto & Dutra (2003) – around Cyg OB2#22 and Cyg OB2#8, respectively. Thus, we adopt 1755^{+23}_{-19} pc from Berlanas et al. (2018) as the distance to Cyg OB2 and J20395358+4222505, where for the error we have adopted their statistical errors. As lower and upper limits in distance, we adopt the values of 1.5 and 2.3 kpc, respectively.

4.2 Extinction and stellar parameters

Given the adopted distance, we can determine the radius taking into account the observed photometry and the extinction. We take the *B* and *V* magnitudes from the UCAC4 catalogue (Zacharias et al. 2013) and the *J*, *H* and K_s magnitudes from the 2MASS catalogue (Cutri et al. 2003). We adopt the extinction law by Maíz Apellániz et al. (2014) (M14), derived for 30 Dor but applicable to Galactic obscured systems, as the same authors have shown. The M14 law leaves the R_{5495} value free (similar but not identical to R_V), which allows us to modify the extinction ratio between different bands. We point out here as a cautionary remark that this extinction law, although using a more extended range of reddening values than any other one, has been derived for extinctions smaller than that of J20395358+4222505.

With the extinction law, and using the magnitudes that come from our final model atmosphere after integrating the emergent flux distribution over the appropriate photometric filters, we can derive the stellar radius and total extinction in any photometric band. We have used the infrared magnitudes to determine the radius, as these are less affected by extinction and are independent of the R_{5495} value adopted. We then use the combined optical and infrared photometry to obtain R_{5495}. For a typical value of $R_{5495} = 3.1$, we find strong differences between the radii derived from the optical (*B*, *V*) and infrared (*J*, *H*, K_s) bands. We find a consistent radius from these bands for $R_{5495} = 2.8^{+0.2}_{-0.1}$, close to the value given by Wright, Drew & Mohr-Smith (2015) ($R_V = 2.9$). With these values, we obtain those quoted in Table 4 for the extinction and find a radius $R = 41.2 \pm 4.0$ $R_\odot$. From here, we derive a luminosity $\log(L/L_\odot) = 5.71 \pm 0.04$, a bolometric magnitude $M_{bol} = -9.52 \pm 0.10$ and a present stellar mass $M = 46.5 \pm 15.0$ $M_\odot$, where the stellar mass has been calculated from the gravity corrected from centrifugal acceleration. The error in the radius, and thus the errors of luminosity, mass and other physical magnitudes, is mainly determined by the inconsistency between the optical and the infrared photometry, as provided here, and not by the adopted uncertainty in the distance. The values corresponding to the lower and upper extreme distances are $R = 34.6$ $R_\odot$, $\log L/L_\odot = 5.55$ and $M = 32.9$ $M_\odot$ (for 1.5 kpc) and $R = 53.5$ $R_\odot$, $\log L/L_\odot = 5.93$ and $M = 77.4$ $M_\odot$ (for 2.3 kpc).

Could a putative companion to J20395358+4222505 affect our determination of stellar parameters? We have chosen HD 2905 to simulate the overlapping of J20395358+4222505 with other stars using spectra from the IACOB data base. With the S/N and resolving power of our observations, we find that at least a conservative

[8]Interestingly, a similar situation arose in DR2 for Cyg OB2#12, the blue hypergiant in the region (see Berlanas et al. 2018) but it has been solved in eDR3

[9]DR2 data give $\langle\mu_\alpha\rangle = -2.109 \pm 0.451$ mas a^{-1} and $\langle\mu_\delta\rangle = 0.073 \pm 0.533$ mas a^{-1} (Berlanas et al. 2020).

[10]Clark et al. (2012) prefer the distance of 1.75 kpc for Cyg OB2 #12 in their analysis.

Table 4. Photometric and extinction values for J20395358+4222505. Photometry is from the UCAC4 and 2MASS catalogues. Maíz Apellániz et al. (2014) has been used for the extinction law.

B	V	J	K_s	R_{5495}	A_B	A_V	A_J	A_{Ks}
16.63	13.682	7.345 ± 0.029	5.822 ± 0.017	$2.8^{+0.2}_{-0.1}$	12.8	9.7	2.8	1.1

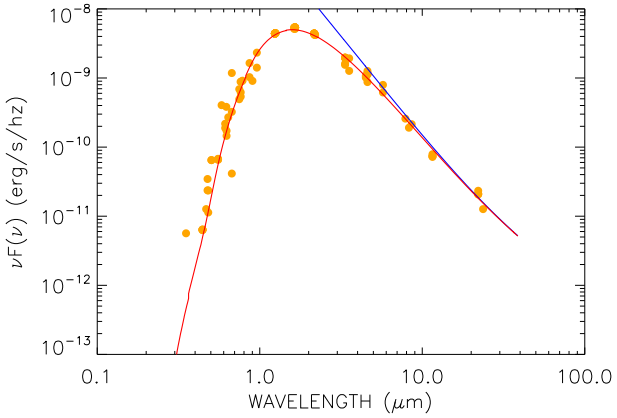

Figure 5. Comparison of the observed photometry from the VizieR Service Photometry Viewer Tool (orange dots; references for the data are given therein) with the continuum flux of our final model, scaled for the adopted distance and corrected from extinction (red line). Because of the hot temperature, only the Balmer jump is clear when plotting the continuum flux in the wavelength region shown. The Paschen jump is present but hard to see in the figure. The blue line is the model flux without the extinction correction, which peaks at around 1100 Å and reaches 6.2×10^{-6} erg s^{-1} Hz^{-1}. See text for details.

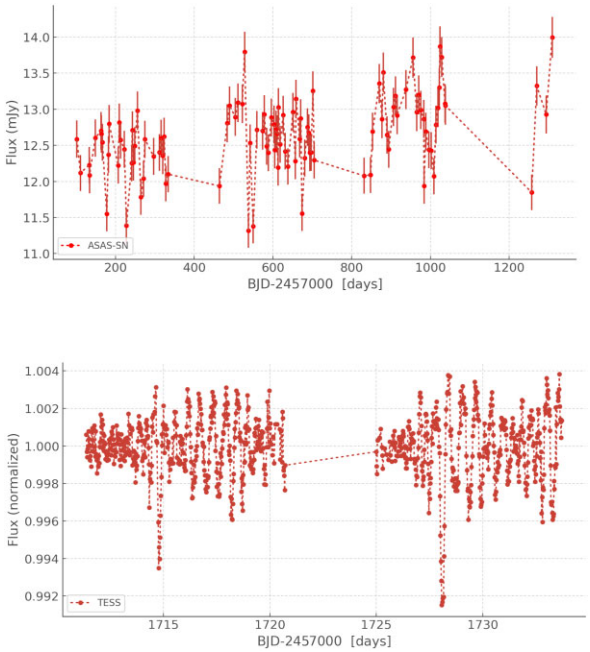

Figure 6. ASAS-SN (top) and *TESS* (bottom) light curves for J20395358+4222505. The variability is clear for both data sets even if the amplitude and time domain differ. The *TESS* light curve has been cleaned of bad data.

flux ratio of 1:0.25 is required for the diagnostic lines to start to be affected. Given the large radius and visual intrinsic brightness of J20395358+4222505, this excludes the possibility of spectral contamination by a hot stripped star or even a hot luminosity class V star, which should be of a spectral type later than O4V (the type of J20395358+4222505 at the zero age main sequence, ZAMS). An evolved secondary should be at least as bright as an O5 III star, but should descend from a star less massive (at ZAMS) than J20395358+4222505, which would imply previous mass transfer and a higher initial mass for J20395358+4222505. Even in this case, the change in the parameters derived from the spectrum would be very small and the effect on radius, mass and luminosity through the change in magnitude would remain within the limits given in Table 2. There is, however, the possibility of a spectroscopically very similar companion, which would not modify the spectroscopic parameters, but would imply a significant change in magnitude (≈0.7 mag.). The radius would be 30 $R_\odot$, with $\log L/L_\odot = 5.43$ and $M = 25.1$ $M_\odot$. The fact that we derive normal abundances for all analysed elements but carbon is also a hint of small, if any, contamination in the spectrum (see section 4 in Lennon et al. 2021) except again for the case of two similar stars.

4.3 Photometric variability

We have compared our model with the existing photometry in the range 0.3–25 μm. Fig. 5 shows the photometric data from the VizieR Service Photometry Viewer Tool (developed by A.-C. Simon and T. Boch; see also Ochsenbein, Bauer & Marcout, 2000), compared to our final model flux with the derived radius, scaled for the adopted distance to Cyg OB2 and J20395358+4222505 and corrected for extinction using the M14 law. We see that the overall agreement is excellent, in spite of the relatively large dispersion in the observed data. This may point towards source variability, although the large extinction, particularly at shorter wavelengths, introduces additional difficulties in the measurements. The good agreement between the model and the observation at larger wavelengths (and the absence of any significant difference with the extinction uncorrected model beyond 10 μm) indicate that there is no emission excess at longer wavelengths due to circumstellar material.

As mentioned before, the B magnitude given by Comerón & Pasquali (2012) from the NOMAD catalogue (Zacharias et al. 2004) and the one used here from the UCAC4 catalogue do not agree. Therefore, we have searched the data bases for variability. No information could yet be extracted from *Gaia*, as the object is not included in the list of targets for which epoch information is available. The information in 2MASS is also very scarce, with only two measurements on the same day with identical values within errors. PanSTARRS provides also a few measurements, but nothing can be concluded from them.

Inspection of the light curves by the ASAS-SN (Kochanek et al. 2017; Shappee et al. 2014) and *TESS* (Ricker et al. 2015) projects (see Fig. 6) reveals variability on the scale of days and years. The ASAS-SN light curve[11] shows a modest increase, of the order of 1 mJy ($\Delta V \sim 0.15$ mag), in the flux of J20395358+4222505 during 3 yr. For

[11] https://asas-sn.osu.edu

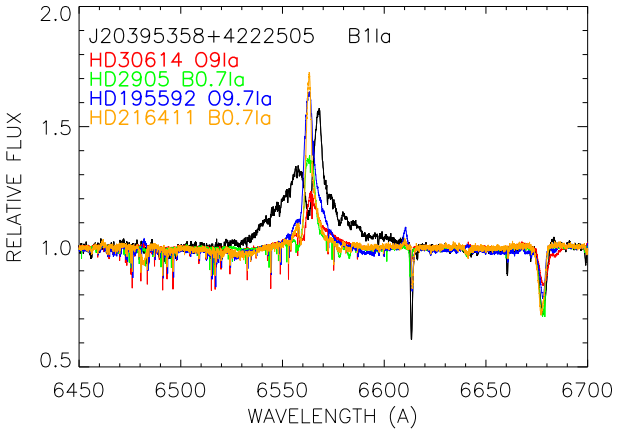

Figure 7. The H_α profile of J20395358+4222505 is compared with some of the strongest profiles in O9-B1 supergiants. Other stars of similar spectral type with strong H_α emission (e.g. HD 104565, OC9.7 Iab, HD 148686, B1Iaeqp, or HD 190603, B1.5Ia$^+$) show the same behaviour as the ones shown here: their H_α profiles are narrower than that of J20395358+4222505 and the emission peaks are usually (not always) lower. The list in the upper-left corner follows the height of the profile peaks.

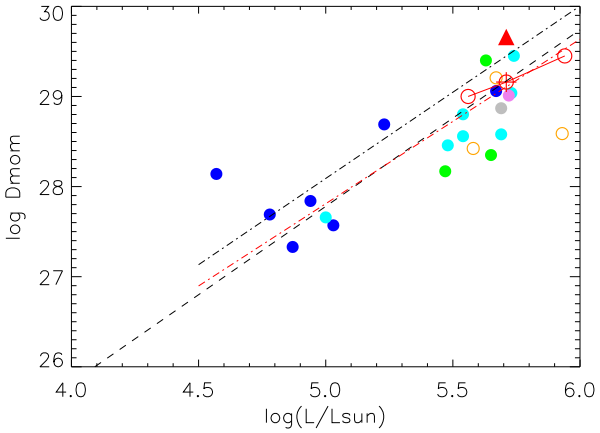

Figure 8. The WLR for B0–B1.5 Galactic supergiants. Solid symbols represent unclumped values, and hollow symbols are for values that include clumping. Data are from Crowther et al. (2006) (green circles, also including the O9.5Ia star HD 30614), Searle et al. (2008) (cyan), Markova & Puls (2008) (magenta), Clark et al. (2012) (orange, hollow circles), Haucke et al. (2018) (blue) and Simón-Díaz et al. (2018) (grey). We also plot the values we obtain for J20395358+4222505 at the different luminosities (hollow red circles) and the unclumped value we obtain for our star at the Cyg OB2 distance (solid red triangle). The cross in the central hollow symbol of J20395358+4222505 gives the size of the error bars. For our star, we have joined the clumped values corresponding to the different distances. The dashed line is the fit obtained by Haucke et al. (2018) to their points and the dash-dotted lines are the relationships obtained by Vink et al. (2000) for Galactic O (red line) and B (black line) stars.

the *TESS* light curve, normalized and detrended by Kepler spline and available at MAST as a High Level Science Product (HLSP[12]; Huang et al. 2020), the observed variability after cleaning the curve of bad data (skipping data with quality flag higher than 2048) is dominated by the variability at the level of ±0.2 per cent in time-scales of about 0.5 d (much shorter than the rotational period of 19.4 × sin*i*), typical of OB supergiants (see, e.g. section 3.6 in Burssens et al. 2020). Two slightly stronger peaks (≈ 1 per cent) are separated by about 13 d. With these two peaks, if the variability were of binary or rotational origin, we would be able to constrain the corresponding inclination, but present data are insufficient to clearly distinguish between the different possibilities (stochastic or pulsational variability, rotational modulation, binarity).

4.4 Wind properties

The H_α emission of J20395358+4222505 is exceptional for its spectral type, as the comparison with HD 2905 in Fig. 3 has shown. In Fig. 7, we compare the H_α profile from J20395358+4222505 with those of the stars showing the strongest emission in a list of 176 Galactic B supergiants currently under analysis (de Burgos et al., in preparation; the sample includes some O9 supergiants). None of the inspected stars displays such a strong H_α profile, although in some cases the emission peak may be higher than that of J20395358+4222505. Even taking into account the variability of this line in B supergiants (see, e.g. Haucke et al. 2018; Simón-Díaz et al. 2018) it is clear that J20395358+4222505 shows a remarkable H_α profile.

The wind has a high terminal velocity compared with stars of the same spectral type (see, e.g. fig. 11 in Clark et al. 2012, where the highest terminal velocity of a B1 supergiant is 1275 km s^{-1} for the peculiar star HD 190066, a value taken from Searle et al. 2008). Its ratio to the escape velocity ($v_\infty/v_{\rm escape} = 2.7$)[13] confirms that the star is still at the hot side of the first bi-stability jump (BSJ), very close to the intermediate zone between the hot and cool sides (see fig. 12 in Markova & Puls 2008; see also Petrov, Vink & Gräfener 2016). The high $v \sin i$ also supports this, as B supergiants on the cool side show lower projected rotational velocities.

The mass-loss rate derived from the stellar parameters we have obtained is $2.4^{+0.2}_{-0.3} \times 10^{-6}$ M$_\odot$ a^{-1}, with values that range between 1.8 and 3.6 × 10^{-6} M$_\odot$ a^{-1} when considering our lower and upper distance limits (the unclumped values would amount to 5.7, 7.6 and 11.4 × 10^{-6} M$_\odot$ a^{-1}). Comparison with fig. 11 of Clark et al. (2012) shows how strong is the wind of J20395358+4222505. This can also be appreciated when comparing with other works in the literature. Benaglia et al. (2007) show that two stars in the $T_{\rm eff} = 20$–25 kK range show an unusual large wind efficiency[14]: HD 2905 and HD 169454 (the latter is one of the hypergiants in the sample of Clark et al. 2012). The wind efficiency we obtain for J20395358+4222505 ($\eta = 0.33$) is comparable to that of those stars in Benaglia et al. (2007) (η =0.4–0.5), and higher if we consider the presence of clumping in our analysis.

In Fig. 8, we plot the modified wind momentum ($D_{\rm mom}$)–luminosity relationship (WLR; Kudritzki, Lennon & Puls 1995) for the B0–B1.5 stars analysed by different authors. We compare it with the one we obtain for J20395358+4222505 at the adopted distance of 1.76 kpc (the dot with the error bars) and at the lower and upper distance limits of 1.5 and 2.3 kpc. The plot includes values for Galactic B supergiants by Crowther, Lennon & Walborn (2006), Searle et al. (2008), Markova & Puls (2008), Clark et al. (2012), Haucke et al. (2018) and Simón-Díaz et al. (2018). Only Clark et al. include clumping as we have done and thus we must be careful with

[12] https://archive.stsci.edu/hlsp/qlp

[13] With $v_{\rm escape}$ corrected for the $(1 - \Gamma_{\rm e})$ factor, where $\Gamma_{\rm e}$ is the ratio of radiation pressure acceleration due to electron scattering to gravitational acceleration.

[14] The wind efficiency is defined as $\eta = (\dot{M} v_\infty)/(L/c)$.

the comparisons. As a reference, we have added the position of our star at the distance of Cyg OB2 when we do not consider clumping (i.e. multiplying by $\sqrt{10}$) and that of the O9.5Ia star HD 30614 from Crowther et al. (2006). Clumped and unclumped values are given by hollow and solid symbols, respectively. We also show the fit obtained by Haucke et al. (2018) to the early B-types (B0–B1.5) in their sample and the WLR predicted by Vink, de Koter & Lamers (2000) for Galactic O and B stars (actually, stars at the hot and cool sides of the BSJ).

We see that the modified wind momentum of J20395358+4222505 agrees well at any distance with the WLR expected for stars at the hot side of the BSJ and with the relationship obtained by Haucke et al. (2018) for their early B supergiants. However, we note that we have included clumping. The modified wind momentum of J20395358+4222505 is also comparable to (or larger than) many unclumped values for B stars in the literature. From the values by Clark et al. (2012) for the early-B hypergiants, only BP Cru (Wray 15-977, also a high-mass X-ray binary) has a comparable modified wind momentum, precisely the star for which Clark et al. (2012) obtain a clumping factor of $f_{\rm cl} = 1$. In contrast, the point representing the unclumped value of J20395358+4222505 lies above any other point, including that of HD 30614, and above the WLR for stars at the cool side of the BSJ. Thus, if our adopted clumping is typical for these stars, J20395358+4222505 has an exceptionally high modified wind momentum and the typical early B supergiants would be below the predicted values.

The actual mass-loss rate of J20395358+4222505 depends of course on the actual clumping structure in the wind, which we have just adopted here. Observations at longer wavelengths will be needed to obtain some information on its clumping, but it is clear that the wind of the star is stronger (i.e. with more momentum) than we would expect from its spectral classification. The H_α profile resembles that of much earlier spectral types (such as mid-O supergiants). We have considered the possibility that the star has an earlier spectral type. For example, we see some weak Si IV and He II 4686Å. However, these features are consistent with a B0.5–B1 classification together with a high luminosity. More importantly, all other spectral features are consistent with the classification (e.g., the ratio of He I to Mg II or the Si spectrum) and imply that the star cannot have an earlier spectral type. The main uncertainty about the strong wind in J20395358+4222505 comes from the H_α variability of B supergiants. Haucke et al. (2018) analyse the variability of Galactic B supergiants and find variations in the H_α profile of all of them, in some cases very significant ones. In the most extreme cases, these variations translate into a factor of 2.7 in the mass-loss rate. If we decrease our mass-loss rate for J20395358+4222505 by such a factor (assuming that we have observed the star during a particularly strong H_α emission phase) we will still have a very strong wind, but not one departing so remarkably from the average behaviour. Clearly, a follow-up spectroscopic campaign is required to solve this issue. Meanwhile, J20395358+4222505 should be included among the stars with a very strong stellar wind (for its spectral classification).

4.5 Evolutionary status of J20395358+4222505

Fig. 9 shows the Hertzsprung–Russell diagram (HRD) with evolutionary tracks from Brott et al. (2011) for an initial rotational velocity of 220 km s^{-1}. We have chosen this value because, at the position of J20395358+4222505 in the HRD, it gives a rotational velocity close to the one observed (≈100 km s^{-1} from the tracks versus $v \sin i = 110$ km s^{-1} observed); we note however, that the actual rotational velocity could be larger, as we do not know the inclination of the rotational axis (see Section 4.3). The position of J20395358+4222505 in the diagram (adopted distance and upper and lower limits) is marked by the red solid circles. The same stars as in Fig. 8 with the same colour codes have also been plotted and we have added the B0–B1.5 supergiants in Cyg OB2, Cyg OB9 and surroundings listed by Berlanas et al. (2018) (open orange circles). We note that these latter authors use calibrations to obtain temperatures and luminosities from the spectral classification, not individual analyses. We have added them because they are in the same region as J20395358+4222505 and probably belong to the same star-forming region (and possibly to the same association). Note also that Berlanas et al. (2018) used a distance modulus of 10.8 mag for Cyg OB2, while we are using 11.2. We then increased their luminosities by 0.16 dex for the stars in Cyg OB2 and their surroundings for the comparison.

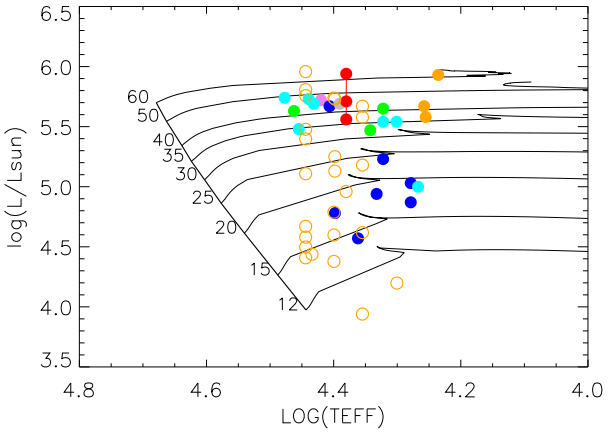

Figure 9. HRD with the position of J20395358+4222505 for the adopted distance and the upper and lower distance limits adopted (solid red circles). The same stars as in Fig. 8 have been plotted, plus the B0–B1.5 supergiants in Cyg OB2, Cyg OB9 and their surroundings by Berlanas et al. (2018) (open orange circles; these are calibrations, see text). The evolutionary tracks have been taken from Brott et al. (2011) for stars with initial rotational velocities of 220 km s^{-1}. The number close to the ZAMS is the stellar initial mass in solar masses.

We find that J20395358+4222505 is a very luminous blue supergiant, comparable to the most luminous of its class and to some of the cooler blue hypergiants, a group that it will possibly join in the course of its evolution. The strong H_α emission, the observed variability and the high luminosity indicate that the star is possibly approaching such a phase.

As in the discussion in the previous section, we plot in Fig. 9 the points corresponding to the distances of 1.5 and 2.3 kpc. At the distance of 2.3 kpc, the luminosity of J20395358+4222505 would be $\log L/L_\odot = 5.93$, placing the star above any other at a similar temperature, consistently with the strong H_α emission observed (we note that H_α variability, or a combination of luminosity and variability, could also be an explanation for the strong H_α emission). Even at a distance as close as 1.5 kpc, the star would have $\log L/L_\odot = 5.55$. The tracks indicate an initial stellar mass around 46.0 $M_\odot$, with a present mass of 39.9 $M_\odot$, slightly lower but consistent with the spectroscopic value we obtained (46.5 ± 15.0 $M_\odot$; note that the mass discrepancy will in this case increase with mass, i.e. with increasing distance). The mass-loss rate predicted by the tracks at the position of J20395358+4222505 is 9.1×10^{-6} $M_\odot a^{-1}$. This is very close to the one we have determined if we neglect the effect of clumping (7.6×10^{-6} $M_\odot$ a^{-1}). This means that the star should

have lost less mass than predicted by the tracks if the effect of clumping remains approximately constant from the ZAMS up to the stage of J20395358+4222505, reducing the difference between the evolutionary and spectroscopic masses. As indicated before, this large mass-loss rate cannot be acting during a long period, except if we assume that the angular momentum is efficiently transported from the interior to the surface (as is predicted by the models of Brott et al. 2011).

The star does not show a CNO pattern as would be expected because of the relatively advanced evolutionary stage. Only a mild C deficiency, based on only one line, is observed, while the N abundance is found to be solar, with the models from Brott et al. (2011) predicting nearly twice this value (8.05 versus 7.83 ± 0.15). The He abundance also does not show indications of enrichment, and the other α elements analysed, Si and Mg, also point to solar abundances. Therefore, in spite of the advanced evolutionary phase and the high rotational velocity (and the possible efficient transport of angular momentum from the interior) we do not see evidence of a significant surface enrichment by hydrogen-burning products. These facts may be consistent with the evolution of a binary system in which J20395358+4222505 would have been the initial secondary (Langer et al. 2020), gaining mass and angular momentum during the mass transfer, but without significant enrichment (a situation that would depend on the characteristics of the binary systems, such as the initial period and mass ratio, and the details of the mass transfer process). This scenario would be supported by the possible radial velocity variations indicated by the *B*-band spectrum, but they require confirmation. We note, however, that the lack of evidence of a runaway nature of J20395358+4222505 increases the chance that, if it initially formed a binary system with a more massive companion, the system is still bounded.

5 CONCLUSIONS

We have analysed J20395358+4222505, a previously known supergiant (initially classified as B0 I) in the neighbourhood of Cyg OB2 and in the direction of the star-forming region DR21. Its high extinction along the line of sight made it inconspicous and concealed its high luminosity. Having realized it (Berlanas et al. 2018), we observed the star during a MEGARA@GTC commissioning run.

We have found a difference in radial velocity between the spectrum taken on the first night of observation and the other spectra taken the night after. We find a small discrepancy between the position of the interstellar lines between those nights, but much smaller than the detected stellar radial velocity variations.

We classify the star as B1 Ia based mainly on its Si spectrum, the emission in H_α and the weakness of the higher Balmer emission lines and of the N II spectrum. The lack of a P-Cygni profile in H_β prevents us from classifying it as Ia^+, and we suggest that this purely spectroscopic criterion should be adopted to distinguish classes Ia and Ia^+. The spectrum shows a very strong H_α emission profile for its spectral type, even when comparing with other early-B Ia supergiants or Ia^+ hypergiants.

The analysis of the spectrum indicates a hot B supergiant with an unusually strong wind (for which we have assumed the clumping factor and characteristics based on the work by Clark et al. 2012), a high projected rotational velocity and solar abundances for all elements, except for a mild C underabundance (based only on the C II 4267 line) and a possible slightly He enrichment (but still compatible with solar). In particular, N is found to be fully consistent with solar. Thus, in spite of the large rotational velocity, the abundance pattern seems to be free of significant enrichment.

The analysis of the star is hampered by the uncertainty in the distance to the star. We discarded the distance derived from the *Gaia* DR2 parallax, and adopted the distance to DR21 (1.5 kpc) as a lower limit and the distance derived from eDR3 as an upper limit. The star is relatively isolated at a separation of 1.5° from the centre of Cyg OB2, which at the distance of this association means a projected separation of about 45 pc. It has a proper motion that is consistent with the Cyg OB2 members. We adopt the distance to Cyg OB2 as the distance to the star, although we note that the connection is not strong and further work is required to probe it.

Using that distance, we derive the radius from the infrared photometry, and then mass, luminosity and mass-loss rate for that same distance. J20395358+4222505 has a very high mass-loss rate for its spectral type of $2.4^{+0.20}_{-0.30} \times 10^{-6}$ $M_\odot$ a^{-1}, where we have considered a clumping factor of $f_{cl} = 10$. The star has a high wind terminal velocity that places it in the hot side of the bi-stability jump. We see that it agrees well with the expected WLR at this hot side. Compared with similar stars in the literature, however, its modified wind momentum is very large if our adopted clumping is typical of early B supergiants, which would mean that the theoretical value is too large for typical B supergiants.

We confirm that J20395358+4222505 is a very luminous ($\log L/L_\odot = 5.71 \pm 0.04$) blue supergiant and we speculate that the star will join the group of B hypergiants in the near future (astronomically speaking). We obtain a spectroscopic mass of 46.5 ± 15.0 $M_\odot$. This is consistent with the evolutionary tracks by Brott et al. (2011), which give an initial mass of 46 $M_\odot$ and a present mass of 39.9 $M_\odot$. The difference between the spectroscopic and evolutionary masses could be reduced if the mass-loss rate adopted by the evolutionary computations (close to the one we obtain neglecting clumping) were lower.

The high rotational velocity indicates that the high mass-loss rate should be recent, or that the angular momentum transport from the interior is very efficient. However, this last possibility is not consistent with the lack of a clear CNO process pattern at the surface. These facts could also be explained with a binary scenario in which J20395358+4222505 would be the initial secondary, assuming that the initial system had the required properties. The presence of a former more massive companion would be consistent with the lack of a peculiar proper motion in J20395358+4222505 and the hints of radial velocity variation found in this work. However, with only one spectrum supporting it, stronger evidence is required to confirm the presence of such a putative companion.

ACKNOWLEDGEMENTS

We would like to dedicate this paper to Simon Clark, our close friend whose inspiration and contribution to the advance on the field of luminous blue variables and early hypergiants has been fundamental.

We want to thank the referee, Dr Ian Howarth, for his careful reading of the manuscript and the very useful report that helped improve this paper and correct mistakes.

We also want to acknowledge fruitful discussions with N. Langer, I. Negueruela, P. Blay and R. Dorda. We thank A. de Burgos for the list of B supergiants and their spectra.

SS-D and AH acknowledge support from the Spanish Government Ministerio de Ciencia e Innovación through grants PGC-2018-091 3741-B-C22 and CEX2019-000920-S and from the Canarian Agency for Research, Innovation and Information Society (ACIISI), of the Canary Islands Government, and the European Regional Develop-

ment Fund (ERDF), under grant with reference ProID2020010016. MG and FN acknowledge financial support through Spanish grant PID2019-105552RB-C41 (MINECO/MCIU/AEI/FEDER) and from the Spanish State Research Agency (AEI) through the Unidad de Excelencia 'María de Maeztu'-Centro de Astrobiología (CSIC-INTA) project No. MDM-2017-0737. SRB acknowledges support by the Spanish Government under grants AYA2015-68012-C2-2-P and PGC2018-093741-B-C21/C22 (MICIU/AEI/FEDER, UE). SRA acknowledges funding support from the FONDECYT Iniciación project 11171025 and the FONDECYT Regular project 1201490. JIP acknowledges finantial support from projects Estallidos6 AYA2016-79724-C4 (Spanish Ministerio de Economia y Competitividad), Estallidos7 PID2019-107408GB-C44 (Spanish Ministerio de Ciencia e Innovacion), grant P18-FR-2664 (Junta de Andalucía), and grant SEV-2017-0709 'Centro de Excelencia Severo Ochoa Program' (Spanish Science Ministry). AGP, SP, AG-M, JG and NC acknowledge support from the Spanish MCI through project RTI2018-096188-B-I00.

This work has made use of data from the European Space Agency (ESA) mission *Gaia* (https://www.cosmos.esa.int/gaia), processed by the *Gaia* Data Processing and Analysis Consortium (DPAC, https://www.cosmos.esa.int/web/gaia/dpac/consortium). Funding for the DPAC has been provided by national institutions, in particular the institutions participating in the *Gaia* Multilateral Agreement.

This research has made use of the VizieR catalogue access tool, CDS, Strasbourg, France (DOI: 10.26093/cds/vizier) and the VizieR Photometry Viewer Tool developed by Anne-Camille Simon and Thomas Boch. The original description of the VizieR service was published in Ochsenbein, Bauer & Marcout, 2000, A&AS, 143, 23.

This publication makes use of data products from the Two-Micron All-Sky Survey (2MASS), which is a joint project of the University of Massachusetts and the Infrared Processing and Analysis Center/California Institute of Technology, funded by the National Aeronautics and Space Administration and the National Science Foundation.

This publication makes use of data products from the *Wide-field Infrared Survey Explorer*, which is a joint project of the University of California, Los Angeles, and the Jet Propulsion Laboratory/California Institute of Technology, funded by the National Aeronautics and Space Administration.

This publication also makes use of data from the *Spitzer*, *TESS*, *AKARI* and *HST* satellites, the Carlsberg Meridian telescope at the ORM, the PanSTARRS telecopes in Hawaii and the NOMAD, APASS and UCAC catalogues, as well as data from the IACOB spectroscopic data base.

DATA AVAILABILITY

The data underlying this article will be shared on reasonable request to the corresponding author

REFERENCES

Abbott B. P. et al., 2016, ApJ, 818, L22
Asplund M., Grevesse N., Sauval A. J., Scott P., 2009, ARA&A, 47, 481
Bailer-Jones C. A. L., Rybizki J., Fouesneau M., Mantelet G., Andrae R., 2018, AJ, 156, A58
Benaglia P., Vink J. S., Martí J., Maíz Apellániz J., Koribalski B., Crowther P. A., 2007, A&A, 467, 1265
Berlanas S. R. et al., 2020, A&A, 642, A168
Berlanas S. R., Herrero A., Comerón F., Pasquali A., Bertelli Motta C., Sota A., 2018, A&A, 612, A50
Berlanas S. R., Wright N., Herrero A., Drew J. E., Lennon D. J., 2019, MNRAS, 484, 1838
Bica E., Bonatto C., Dutra C. M., 2003, A&A, 405, 991
Brott I. et al. 2011, A&A, 530, A115
Burssens S. et al., 2020, A&A, 639, A81
Cardiel N., Pascual S., 2018, guaix-ucm/megaradrp-calibrations: release 2018.1. Zenodo. Available at: https://doi.org/10.5281/zenodo.2270518
Clark J. S., Najarro F., Negueruela I., Ritchie B. W., Urbaneja M. A., Howarth I. D., 2012, A&A, 541, A145
Comerón F., Pasquali A., 2012, A&A, 543, A101
Crowther P. A., Lennon D. J., Walborn N. R., 2006, A&A, 446, 279
Cutri R. M. et al., 2003, yCat, II/246
de Mink S. E., Langer N., Izzard R. G., Sana H., de Koter A., 2013, ApJ, 764, 166
Gaia Collaboration (A. G. A. Brown et al.), 2018, A&A, 616, A1
Gaia Collaboration (A. G. A. Brown et al.), 2021, A&A, 641, A1
Gaia Collaboration (T. Prusti et al.), 2016, A&A, 595, A1
Gil de Paz A. et al., 2018, Proc. SPIE, 10702, 1070217
Gray D. F., 2008, The Observation and Analysis of Stellar Photospheres. Cambridge Univ. Press, Cambridge
Hanson M. M., 2003, ApJ, 597, 957
Haucke M., Cidale L. S., Venero R. O. J., Curé M., Kraus M., Kanaan S., Arcos C., 2018, A&A, 614, A91
Herbig G. H., 1995, ARA&A, 33, 19
Huang C. X. et al., 2020, Res. Not. Am. Astron. Soc., 4, 204
Kochanek C. S. et al., 2017, PASP, 129, 104502
Kudritzki R.-P., Lennon D. J., Puls J., 1995, in Walsh J. R., Danziger I. J., eds, Science with the VLT. Springer, Berlin, p. 246
Langer N. et al., 2020, A&A, 638, A39
Langer N., 2012, ARA&A, 50, 107
Lennon D. J. et al., 2021, A&A, 649, A167
Lesh J. R., 1968, ApJS, 17, 371
Lindegren L. et al., 2018, A&A, 616, A2
Lindegren L. et al., 2021, A&A, 649, A4
Maíz Apellániz J. et al., 2014, A&A, 564, A63
Maíz Apellániz J., Crespo Bellido P., Barbá R. H., Fernández Arana R., Sota A., 2020, A&A, 643, A138
Markova N., Puls J., 2008, A&A, 478, 823
Massey P., Thomson A. B., 1991, AJ, 101, 1048
Motte F., Bontemps S., Louvet F., 2018, ARA&A, 56, 41
Negueruela I., Marco A., Herrero A., Clark J. S., 2008, A&A, 487, 575
Ochsenbein F., Bauer P.& Marcout J., 2000, A&AS, 143, 23
Pantaleoni González M., Maíz Apellániz J., Barbá R. H., Reed B. C., 2021, MNRAS, 504, 2968
Pascual S., Cardiel N., Gil de Paz A., Carasco E., Gallego J., Iglesias-Páramo J., Cedazo R., 2019, in Montesinos B., Asensio Ramos A., Buitrago F., Schödel R., Villaver E., Pérez-Hoyos S., eds, Highlights on Spanish Astrophysics X. Springer, Berlin, p. 227
Petrov B., Vink J. S., Gräfener G., 2016, MNRAS, 458, 1999
Puls J., Urbaneja M. A., Venero R., Repolust T., Springmann U., Jokuthy A., Mokiem M. R., 2005, A&A, 435, 669
Ricker G. R. et al., 2015, JATIS, 1, 014003
Rivero-González J. G., Puls J., Najarro F., 2011, A&A, 536, A58
Rygl K. L. J. et al., 2012, A&A, 539, A79
Sana H. et al., 2012, Science, 337, 444
Santolaya-Rey A. E., Puls J., Herrero A., 1997, A&A, 323, 488
Searle S. C., Prinja R. K., Massa D., Ryans R., 2008, A&A, 481, 777
Shappee B. J. et al., 2014, ApJ, 788, 48
Simón-Díaz S., Aerts C., Urbaneja M. A., Camacho I., Antoci V., Fredslund Andersen M., Grundahl F., Pallé P. L., 2018, A&A, 612, A40
Simón-Díaz S., Castro N., Garcia M., Herrero A., Markova N., 2011, BSRSL, 80, 514
Simón-Díaz S., Herrero A., 2014, A&A, 582, 135
Simón-Díaz S., Pérez Prieto J.A., Holgado G., de Burgos A., IACOB Team, 2020, Contributions to the XIV.0 Scientific Meeting (virtual) of the Spanish Astronomical Society. Available at: https://www.sea-astronomia.es/reunion-cientifica-2020
Skrutskie M. F. et al., 2006, AJ, 131, 1163

Torres-Dodgen A. V., Tapia M., Carroll M., 1991, MNRAS, 249, 1
Vink J. S., de Koter A., Lamers H. J. G. L. M., 2000, A&A, 362, 295
Walborn N. R., 1972, AJ, 77, 312
Walborn N. R., Fitzpatrick E. L., 1990, PASP, 102, 379
Wright N. J., Drew J. E., Mohr-Smith M., 2015, MNRAS, 449, 741
Zacharias N., Finch C. T., Girard T. M., Henden A., Bartlett J. L., Monet D. G., Zacharias M. I., 2013, AJ, 145, 44
Zacharias N., Monet D. G., Levine S. E., Urban S. E., Gaume R., Wycoff G. L., 2004, AAS, 205, 48.15

This paper has been typeset from a TEX/LATEX file prepared by the author.